ACCESS
Arctic Climate Change
Economy and Society

Project no. 265863

ACCESS

Arctic Climate Change, Economy and Society

Instrument: Collaborative Project
Thematic Priority: Ocean.2010-1 "Quantification of climate change impacts on economic sectors in the Arctic"

D1.22 – Report on Jul/Aug 2012 melt pond statistics and thermodynamics, fed to WP1 modelling for use in predicting accelerated decay

D. Divine, M. Granskog, S. Hudson, C. Pedersen, S. Gerland, T.I. Karlsen and H.-F. Aas

Due date of deliverable: **30/04/2013**
Actual submission date: **01/05/2013**
Used Person/months: 21.5

Project co-funded by the European Commission within the Seventh Framework Programme (2007-2013)		
Dissemination Level		
PU	Public	X
PP	Restricted to other programme participants (including the Commission Services)	
RE	Restricted to a group specified by the consortium (including the Commission Services)	
CO	Confidential, only for members of the consortium (including the Commission Services)	

Start date of project: **March 1st, 2011** Duration: **48 months**

Organisation name of lead contractor for this deliverable: **NPI**

Contents

Table of Contents

Contents

1. Report summary

A new thin-ice Arctic paradigm requires reconsideration of the set of parameterizations of mass and energy exchange within the ocean-sea-ice-atmosphere system used in modern coupled general circulation models (CGCMs) including Earth System Models (ESM), the primary model of the ACCESS project. Such a reassessment would require a comprehensive collection of measurements made specifically on first-year pack ice with a focus on summer melt season when the difference from typical conditions for the earlier multi-year Arctic sea ice cover becomes most pronounced.

This report presents the results from the analysis of data relevant in the context of ACCESS project which was collected by scientists of the Norwegian Polar Institute (NPI) during the field campaign in summer 2012 in the high Arctic to the north of Svalbard. The report focuses on melt ponds - the objects on sea ice surface inherent to the period of melt. The formation of melt ponds on summer sea ice is accompanied by a pronounced decrease of surface albedo leading to an accelerated structural disintegration and decay of melting ice. It is considered that insufficient representation of summer melt processes in modern CGCMs can partly be responsible for their inability to adequately describe the present day accelerated shrinkage of summer Arctic sea ice cover. The presented results comprises data on smaller scale surface topography and optical properties of sea ice in the advanced stage of melt collected *in situ* during an 8-day long ice station in first year Arctic sea ice during 26.07-03.08.12. Together with a standard set of meteorological observations and the oceanic flux measurements proving the estimates of the overall energy budget, the results are intended to aid in improving the CGCMs sea ice scheme for the period of summer melt. The local observations are complemented by the regional scale spatial statistics on melt pond coverage and open water fraction inferred from the four presently processed helicopter survey flights comprising in total some 250 km of flight tracks in the study area covering some 10 km^2 of sea ice surface.

2. Overview of NPI field activities and the project relevant data collected in the Arctic in 2012 spring and summer seasons

During spring and summer of 2012 the scientists from NPI took part in three major field campaigns aimed on the study of the physical properties of Arctic first year sea ice. Especial focus was put on the processes of summer melt and decay, specifically melt ponds, which are important for the transmission of solar energy into sea ice and to the ocean below the sea ice cover.

In late March in collaboration with scientists from CRREL (USA) a study site was established on level landfast ice off Point Barrow in Alaska, USA. A sled based mobile scientific platform ("radiation sled", See Section 3.1) was deployed to study seasonal changes in the optical properties and topography of sea ice surface. The site was regularly revisited later during May-June 2012 with almost daily measurements along the transect during the period of surface melt. The Barrow campaign was not terminated until fast ice became unsafe to work on in mid June, yielding a detailed record of the surface topography, melt pond area,

ice/snow albedo and transmissivity of sea ice from winter conditions to melt onset, melt pond formation and evolution.

The July – August combined ICE12/ACCESS cruise onboard R/V "Lance" featured an eight-day ice station in first-year Arctic drift ice north of Spitsbergen at ca. 82-83°N during 26.07-3.08.2012. The major objective of this cruise was to collect the first complete set of measurements of the energy balance of the current thin first-year sea ice in the high Arctic during summer melt. A set of various sensors mounted on a 5-m long submerged mast provided the data on heat flux from the ocean to the bottom of the ice. The on-ice measurements were carried out with a radiation sled to measure the surface radiation energy balance and an automatic weather station to measure the other atmospheric heat fluxes. At two selected sites a rotary laser was used for mapping the smaller scale sea ice surface topography including melt ponds. The diving team worked in parallel along some selected transects quantifying the light transmission through ponded sea-ice. Regional scale ice thickness variability, sea ice topography and melt pond fraction were studied from helicopter equipped with EM-bird instrument and ICE stereocamera system (Section 3.2).

Later in August-September during another R/V "Lance" cruise in Fram Strait at some 79°N , additional ice reconnaissance flights were undertaken to study the state of sea ice cover during the end of seasonal melt. The flight tracks cover the transect extending from the marginal ice zone to the fast ice/drift ice close to the coast of Greenland.

Table 1 gives the overview of the collected data together with its current status.

Table 1 Summary of ACCESS project relevant data collected and calculated during the spring and summer 2012 NPI field campaigns in the Arctic

Data category	Variable	Period and location	Current data status
Local meteorological and oceanographic data; radiation fluxes	2m air temperature, humidity, wind speed, depth profiles of water temperature and salinity, net incoming and outgoing longwave and shortwave radiation Turbulent latent and sensible atmospheric heat fluxes, oceanic turbulent heat flux	27.03-03.04.12; 15.05-15.06.12; Point Barrow, Alaska, USA 26.07.-03.08.12; 82.5°N during drift north of Svalbard (see report text for more details on the location);	Data partly processed
Sea ice surface topography and surface types classification	Fractional coverage for different surface classes (bare ice, open water, melt pond)	24.07.-03.08.12; 82.5°N north of Svalbard; 12 ice reconnaissance flights 20.08-02.09.12; Fram Strait at 79°N north; 11	Data from 4 of 12 flights processed Not processed

		reconnaissance flights	
	Morphological properties of melt ponds		*in situ* collected data processed (see text for details)
	Surface roughness		Not processed
	Ice ridge density, sail height		Not processed
	Floe size distribution in the marginal ice zone		Not processed
Optical properties of sea ice	Surface spectral and broadband albedo for first year ponded and bare ice	27.03-03.04.12; 15.05-15.06.12; Point Barrow, Alaska, USA	Data partly processed
	Ice spectral and broadband transmittance through the bare ice and beneath melt ponds	26.07.-03.08.12; 82.5°N during drift north of Svalbard	
Atmospheric and oceanic heat fluxes	Turbulent latent and sensible atmospheric heat fluxes, oceanic turbulent heat flux (ICE12 cruise only)	27.03-03.04.12; 15.05-15.06.12; Point Barrow, Alaska, USA	Data partly processed
		26.07.-03.08.12; 82.5°N during drift north of Svalbard	

3. Instrument setups used for studing the morphological and optical properties of melt ponds

3.1 Radiation sled - intergrated platform for measuring the optical properties of sea ice surface

Figure 1 Measuring the optical properties of a melt pond using the radiation sled. Photo: Tor Ivan Karlsen (NPI).

The “radiation sled” (setup deployment shown in Figure 1) is an integrated instrument package designed at NPI for measuring the surface radiation budget of sea ice (Hudson et al., 2012). The setup simultaneously measures broadband fluxes of upwelling and downwelling terrestrial and solar radiation (four components separately), spectral fluxes of incident and reflected solar radiation, and supporting data such as air temperature and humidity, surface temperature, and GPS location, in addition to photographing the sky and observed surface during each measurement. It is mounted on a sled with floatation capability, allowing measurements of the radiation budget to be made at many locations in the study area including the melt ponds themselves. The use of the setup enables studying the effect of small-scale surface processes on the large-scale surface radiation budget.

The instruments presently mounted on the sled include: *Kipp & Zonen CNR4* four-component net radiometer to observe broadband upwelling and downwelling shortwave (solar) and longwave (thermal terrestrial) radiation; a single-channel *ASD FieldSpec Pro* spectroradiometer to observe spectral albedo and calibrated solar fluxes at wavelengths from 350 to 2200 nm; web-cameras to take surface and sky photos at the time of each observation. Surface (skin) temperature observed with a *Campbell IR-120* infrared thermometer, air temperature and humidity registered with a *Vaisala HNP45* sensor, and time and location from GPS.

The setup was deployed for the first time in June 2011 on fast ice offshore from Point Barrow, Alaska and after some modifications/improvements used again during the Point Barrow 2012 spring and summer field campaigns and ICE12/ACCESS research cruise.

3.2 ICE stereocamera – the helicopter borne system for mapping the surface topography and surface types classification.

3.2.1. Hardware setup

One of NPI's major contributions in the framework of ACCESS project during 2011-2012 was a development of a helicopter borne ICE stereocamera system – a photogrammetric setup intended for a small scale (< less than a decimeter) mapping of the sea ice surface topography and aerial photography. The data retrieved by the camera system can also be used for detection of the state of sea ice cover along the flight track, i.e. classification with respect to the predefined set of surface types.

The hardware component of the system comprises two Canon EOS 5D Mark II digital photo cameras equipped with Canon 20 mm f/2.8 USM lenses, combined SPAN-CPT GPS/INS unit by "Novatel" and the laser distance measurement device LDM301 by "Jenoptik". These components together with the DC/DC converter are housed in a single aerodynamic enclosure designed and manufactured by "Tronrud Engineering AS" and mounted outside the helicopter on AFSP-1 single pole utility mount (Figure 2). The cameras are positioned with a horizontal image axes oriented along the flight direction to ensure the highest possible overlap between the successive images.

In order to minimize the effect of vibrations on the system performance its rigid inner bearing frame is attached to the aerodynamic enclosure via antivibration spring pads (Figure 2). The unit is controlled by a "National Instruments" PXI chassis mounted inside the helicopter cabin. "Novatel" ANT-A72GLA-TW-N GPS antenna was mounted on the roof of the helicopter cabin; the respective lever arm between the antenna phase centre and the GPS/INS enclosure centre of navigation was measured with a high accuracy.

When on the ground and during takeoffs/landings the camera lenses are closed by a rotating electromechanical hatch to prevent snow/dust contamination of the optical surfaces. The hatch opening/closing is controlled manually by an operator in the helicopter cabin.

The entire system is powered by the onboard helicopter DC 24 V power in the flight mode. The external standard 220 V AC power and the AC/DC converter are used when the helicopter is in the parking position.

We note that the use of components in the system design mostly available on the consumer market and NPI own software resources ensured a fairly competitive price on the whole system compared with other commercial photogrammetric setups available on the market.

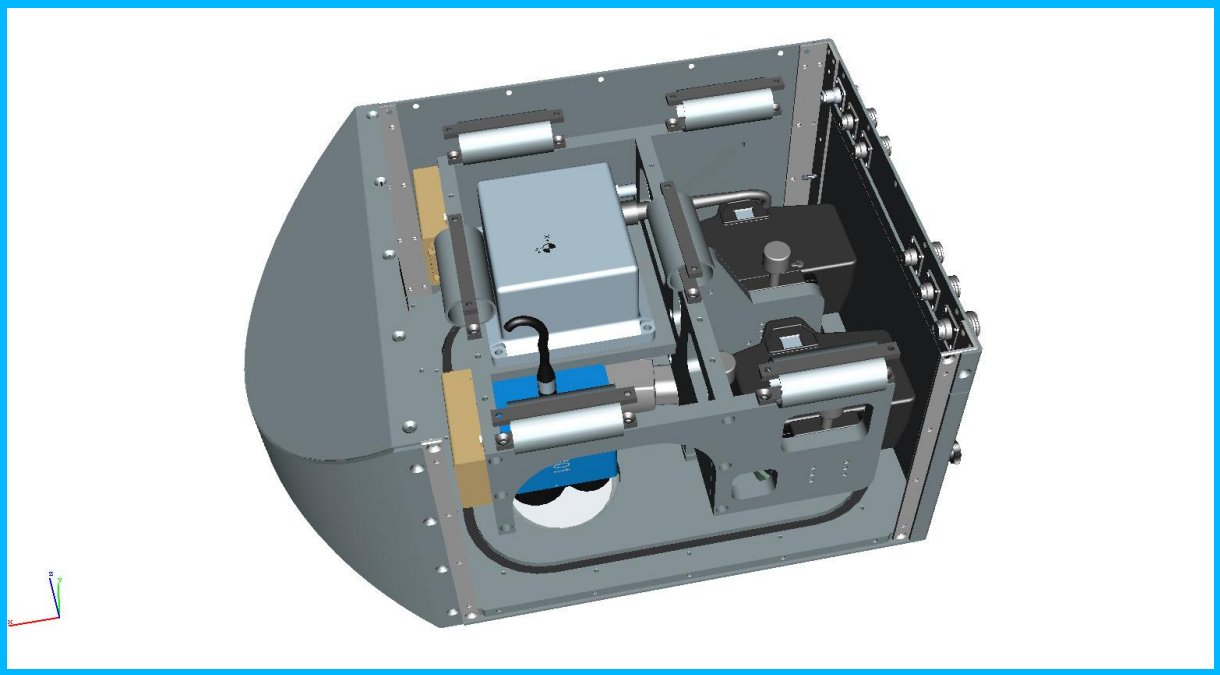

Figure 2 Top left panel: ICE stereocamera system mounted on the helicopter using a single pole utility mount (left panel); **Top right panel**: rear view of the camera system house with the back panel off showing two Canon Mk II photo cameras; note antivibration mounts in the top of the main inner frame. **Bottom panel** shows housing of the instruments inside the aerodynamic enclosure.

3.2.2. Camera system operation and data acquisition.

Switching of the ICE stereocamera system from the “ground” to the “flight mode”, i.e. when the cameras are capturing images and GSP/INS unit logs the system coordinates, occurs automatically. The mode is triggered by the laser altimeter upon the crossing of the threshold altitude which is now set to 5 m.

PXI chassis controls the shooting rate which is now set to 1 frame per second per camera yielding 2 captured images per second. This is sufficient to ensure some 70% overlap between successive images for the flights at the altitudes of about 35-40 m and with velocity of 30-40 m/sec – parameters typical for the EM-bird flights. The camera shutters are triggered by the input signals from the PXI chassis. Rising edge of the current opening the camera shutters is used as a mark input trigger on the GPS/INS unit and the laser altimeter; position, attitude and altitude of the event is then logged in the system.

The captured images are stored in the cameras own 128 Gb compact flash cards. The cards size is sufficient for the system to shoot continuously for about an hour taking in total some 4500 images per camera in raw Canon format. The system is serviced after every deployment; the images are moved to the HDD storage and backed up, the flash cards formatted.

3.2.3 Image and navigation data processing

For a typical flight altitude of about 35 m the camera lenses and CCD geometry at its native resolution provide a pixel size on the ground and hence a theoretical accuracy of about 1 cm. High positioning accuracy especially with relation to the system altitude is crucial for a successful solution of the stereo matching problem and building the digital elevation model

(DEM) of the underlying surface. A declared single point accuracy of 1.5 m combined with the laser altitude data appeared to be sufficient for a successful solution of the 3D problem. For the next (2013) field season the modifications to the camera software will be introduced to ensure a possibility for further post-processing of the navigation data to attain a positioning accuracy better than 0.2 m. Post-processing will be performed by TerraPos software which can handle both GPS and INS raw data in parallel to yield a combined refined estimate of the system position.

Image correction for camera lens distortion is necessary prior to any further analysis of the acquired images. We used a target-based camera calibration procedure implemented in the PhotoModeler software package to estimate the camera models.

Image processing is organized in two major workflows. Correction for lens distortion and vignetting, image rectification/mosaicing and DEM building is done by SOCET SET photogrammetric software package. Refraction at water/air interface is to be taken into account, providing the data on melt pond coverage, depth and melt ponds bottom topography – the primary goals for the system at its present stage. Analysis of the images in two dimensions as well as statistical processing of the derived DEMs is implemented in the Matlab environment.

The ICE stereocamera system was deployed for the first time during the 2012 July-August ICE12/ACCESS cruise to the north of Svalbard and August-September cruise in Fram Strait. The hardware setup has proven to be highly reliable and was used in 23 helicopter flights over Arctic sea-ice. Being highly automated it required a minimal human supervision during in-flight operation. The deployment of the camera system was mostly done in combination with the EM-bird, which measures sea-ice thickness, to provide an integrated view of sea ice cover along the flight track. Some 70000 images of sea ice/water surface captured per camera sums into 5 Tb of data collected during its first field season.

4. Morphological characteristics of melt ponds on first year Arctic sea ice

4.1 Results of ICE12/ACCESS cruise

Knowledge of the morphological characteristics of melt ponds is of importance for the assessment and modeling the optical properties as well as other physical properties of the upper sea ice surface. Spatial distribution of melt ponds may also have implications for remote sensing of sea ice cover during the period of seasonal melt. A comprehensive set of observations on melting Arctic first year sea ice surface topography and energy was conducted during an eight-day ice station, 26 July to 3 August 2012, in an area of very close (>90%) drift ice north of Spitsbergen during the joint ICE12/ACCESS expedition on R/V *Lance*, in the southwestern Nansen Basin (82.25 N, 21.50 E). The ice floe had a size of approximately 600m and a modal ice thickness of 0.8 m. Based on airborne surveys of ice thickness using the EM-bird instrument and the aerial photography it was found representative for the area. The sea ice was in the later stages of melt with some of the ponds actually melted through the ice slab.

Figure 3 shows ICE12 floe drift track together with the four selected helicopter flight tracks when ICE stereocamera system was deployed. Results of the data analysis from these flights together with *in situ* observations are reported below.

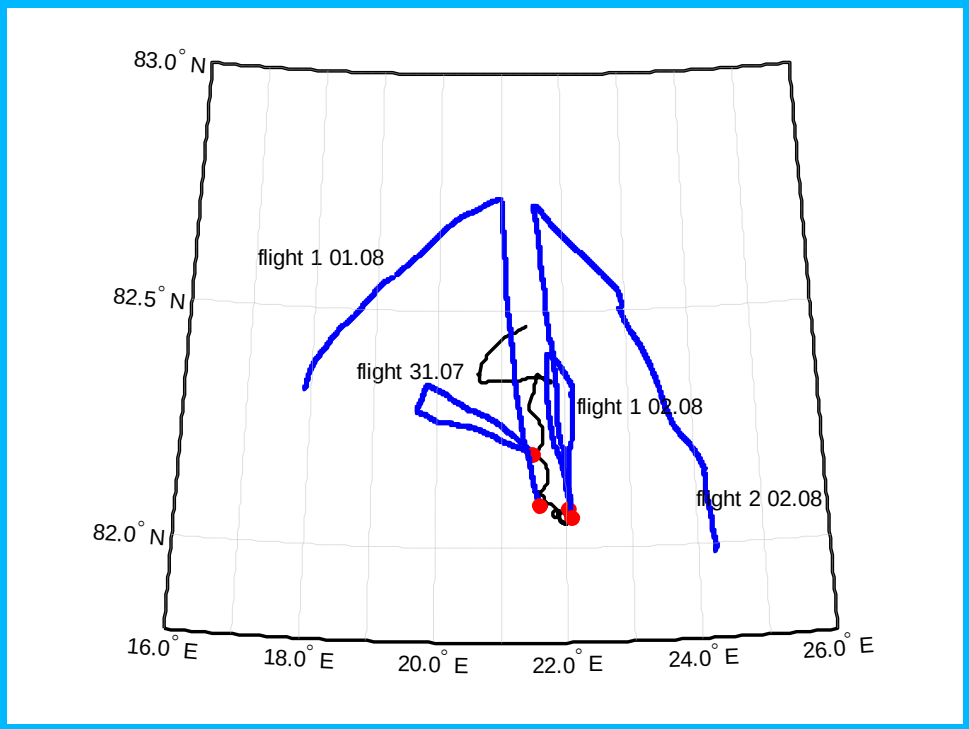

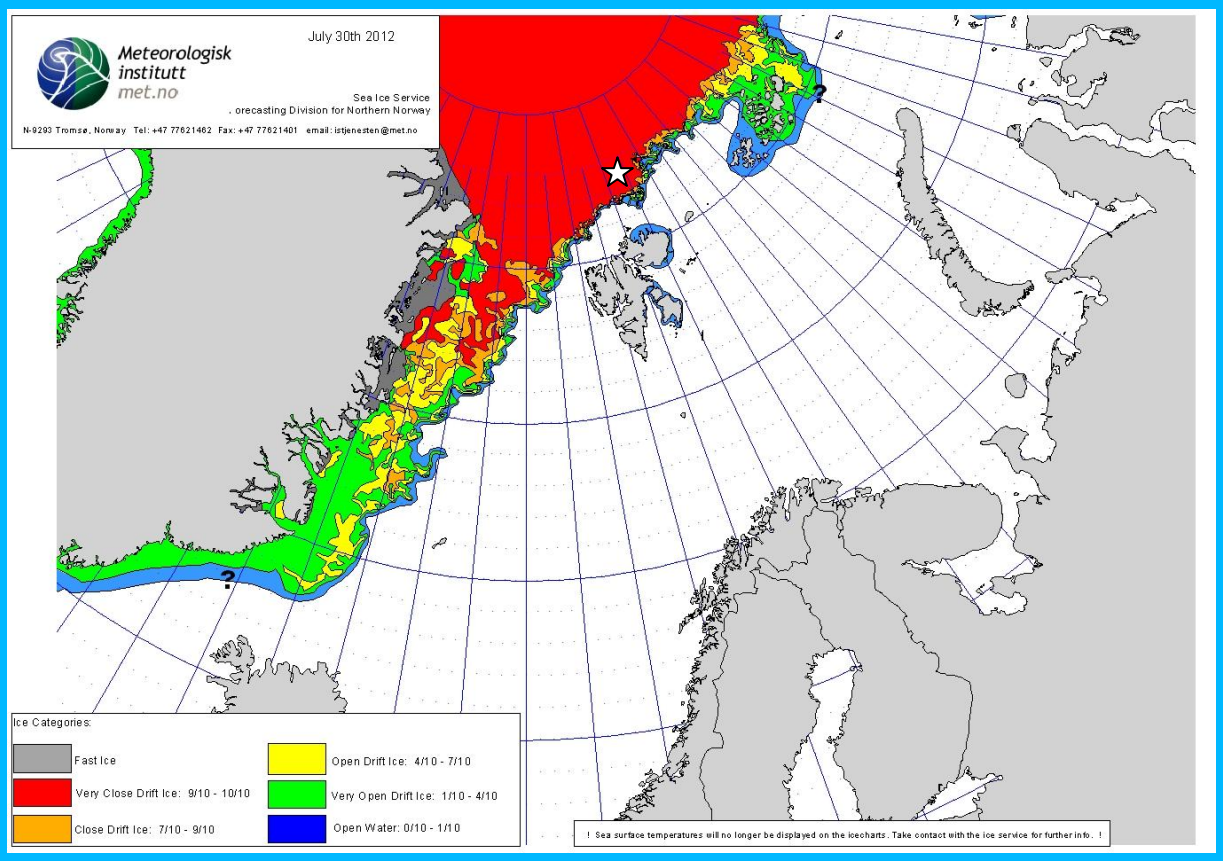

Figure 3, Top: Tracks of ICE12 floe drift north of Svalbard 26 July to 3 August 2012 (black) and four selected helicopter ice reconnaissance flights (blue), red dots mark the starting points for the flights; the data summary on the state of sea ice cover inferred from ICE stereocamera system for these flights presented in Section 5.3. **Bottom**: ice chart of the Norwegian Meteorological Institute for

30.07.2012 featuring a very close drift ice with sea ice concentrations above 90% in the study area (highlighted white star).

4.2 Mapping ponded Arctic first year sea ice topography using rotary laser measurements

The smaller scale sea ice surface topography was studied *in situ* using a rotary laser system, this also provides a validation data for the stereocamera system. The self-levelling rotary laser head was mounted on a tripod on the level sea ice surface during the ICE12 cruise ice station. The established 80 by 80 m topography site (see object 11 “TOPO-site” in Figure 4) was found to be representative of the study area featuring well developed and newly formed melt ponds, bare level ice and two minor ice ridges. The surface elevations were measured relative to the water level which was constantly controlled in order to account for the slow sinking of the tripod. Figure 5 shows the images of the sea ice surface of the TOPO site taken *in situ* during the mapping. In addition to the measurements on a regular 2-meter grid we registered the coordinates and elevations of pronounced topographic features like edges of melt ponds and local elevation maximums.

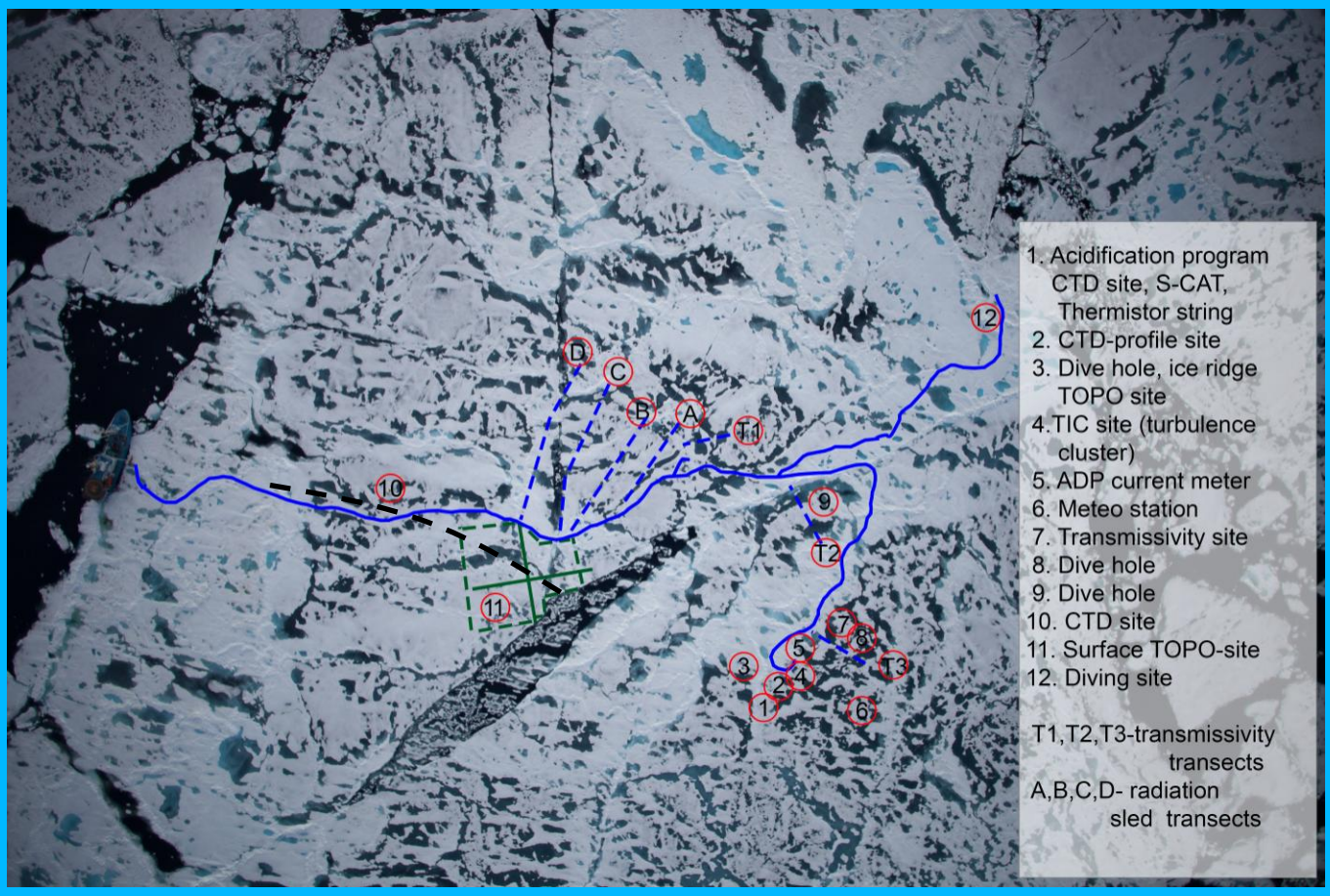

Figure 4. Aerial photo of the ICE12 cruise ice floe used for an 8 days long ice station showing locations of different study sites. Black dashed line depicts the helicopter flight track over the area used as an example of 3D reconstructions of sea ice surface topography in **Section 4.5.**

Figure 5 showing measuring the sea ice topography using rotary laser system (image courtesy Tor Ivan Karlsen, NPI).

Mapping of the surface elevation at the TOPO-site took some 2 days which was considered to be short enough to discard possible topography changes due to sea ice melt. We estimate the elevation measurement error to lie within 2 cm and a spatial error to be less than 20 cm.

Figure 6 presents results of the TOPO site sea ice surface mapping. Most of the melt ponds of the topography site formed a system of channels connected with a large opening in the centre of the ICE floe; the reference water level was therefore set to 0. Only a few minor and shallow (< 5 cm deep) melt ponds at the TOPO site were isolated, however their surface water levels were found to be equal to the reference water level within the measurement error.

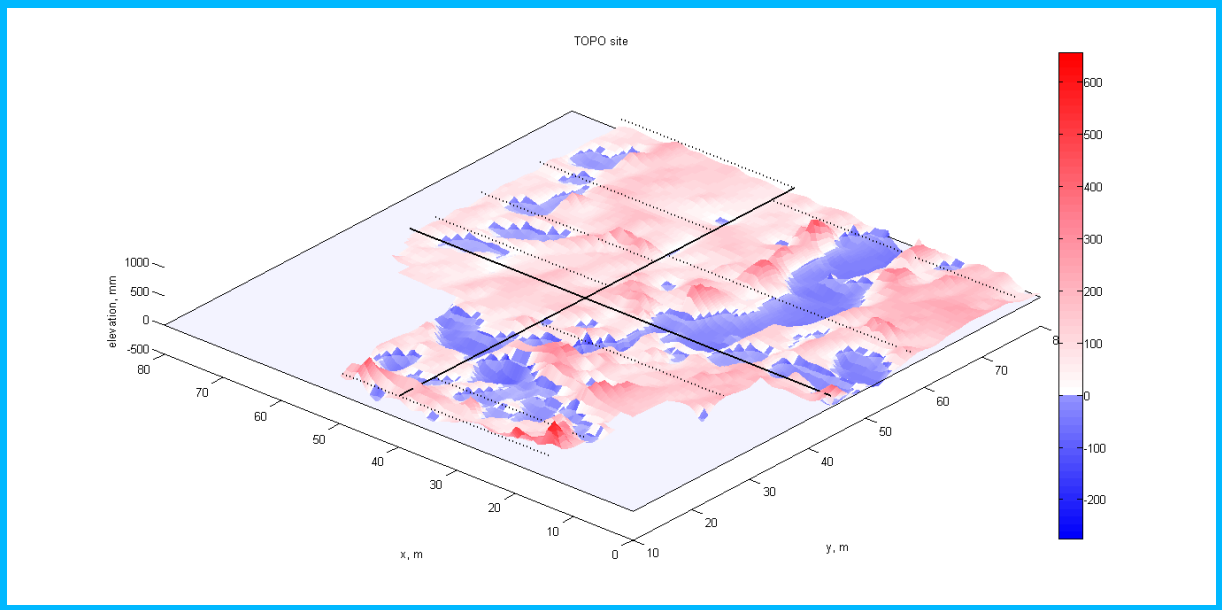

Figure 6. "TOPO site" elevation map featuring the system of connected and isolated melt ponds. The solid black lines highlight the major axes (also indicated by the straight solid lines in **Figure 4**, site 11)

The average melt pond coverage for the topography site was calculated to be about 20% which is similar to the estimates made for the whole ICE12 floe (see below). The average depth of melt ponds in Figure 6 is 10 cm with the maximum registered depth of about 28 cm. Figure 7 suggests, however, the average depth at the TOPO site is not a representative value as the melt ponds tended to be relatively shallow, below 7 cm, or had depths in the interval of 15-20 cm.

In order to check if this inference can potentially be extended to other locations of the ICE floe we analyzed the melt pond depths along four radiation sled tracks (Figure 4**,** tracks A,B,C,D) and three transmissivity sites T1, T2, T3 on different locations on ICE12 floe. Results for tracks A,B,C and D yielded an average depth of 14±5 cm but representativeness of this value is difficult to assess due to a relatively low (20) number of measurements made with a 5 m step along the sled lines that were ponds.

The corresponding stake measurements of melt pond depth and sea ice thickness made with an increment of 1 m along T1, T2 and T3 lines with well developed melt ponds provided an average depth of 17±7 cm. This is much in agreement with the results of the TOPO site (see Figure 7 and depiction of T1,T2 and T3 transects profiles in Figure 21)**,** suggesting a value within 15-20 cm can be regarded a realistic estimate of the melt pond depth on first year pack ice in advanced stages of melt.

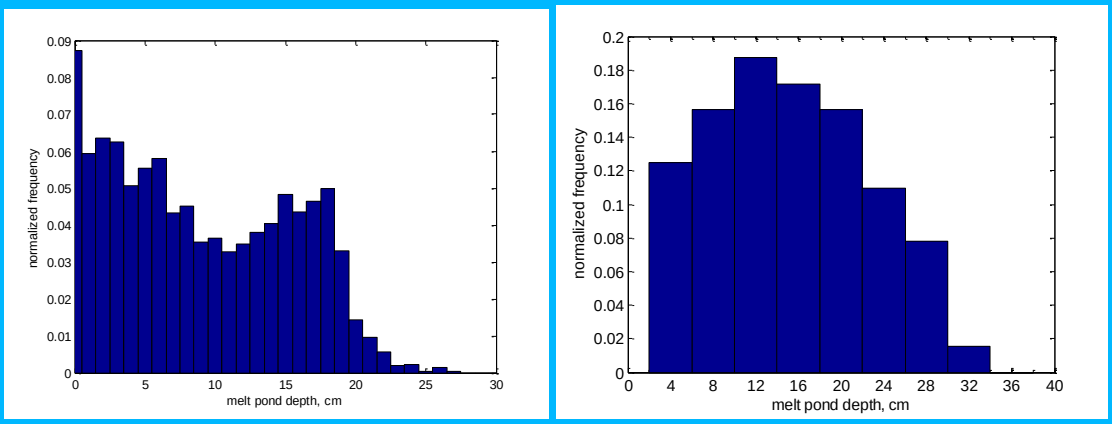

Figure 7. Distribution of melt pond depths measured at TOPO site (left) and T1, T2 and T3 transects (right) during the ICE 2012 cruise.

4.3 Local and regional scale spatial characteristics of melt ponds and melt pond coverage inferred from helicopter borne imagery

This section presents the summary statistics on melt pond coverage and sea ice/open water fractions inferred from the analysis of images acquired by ICE stereocamera system during 4 selected helicopter flights made in ICE 2012 summer cruise.

A majority of flights were made in combination with EM-bird what conditioned the flight altitude to remain within 35-40 m except for some shorter periods of climbing to 150-200 m for conducting the EM-bird calibration procedure. However, a flight around ICE12 floe at 500 m altitude was made on 28.07.12 in order to get an overview of the state of sea ice cover in the area of the ice station. Figure 8 presents the mosaic of images for this flight comprising the swath of approximately 1.2 km long and 0.8 km wide. The size of a pixel on the ground for these rectified images corresponds to 0.1 m.

The object identification is a three-step procedure involving a) image segmentation/binarization using Otsu's method, which chooses the threshold to minimize the intra-class variance of the black and white pixels (Otsu, 1979), b) boundary tracing on the binarized images by the Moore-Neighbor tracing algorithm modified by Jacob's stopping criteria (Gonzalez et al., 2004) and c) object classification (open water or melt pond) using thresholding in the red channel intensity.

Figure 9 demonstrates an example of the object identification procedure for the segment of ICE12 floe, specifically the area labelled 1 to 8 in Figure 4 where most of the stationary instruments for measuring the sea ice energy budget were set up. The melt pond edges are accurately identified; bold contours highlight one particular larger melt pond formed by a system of interconnected channels.

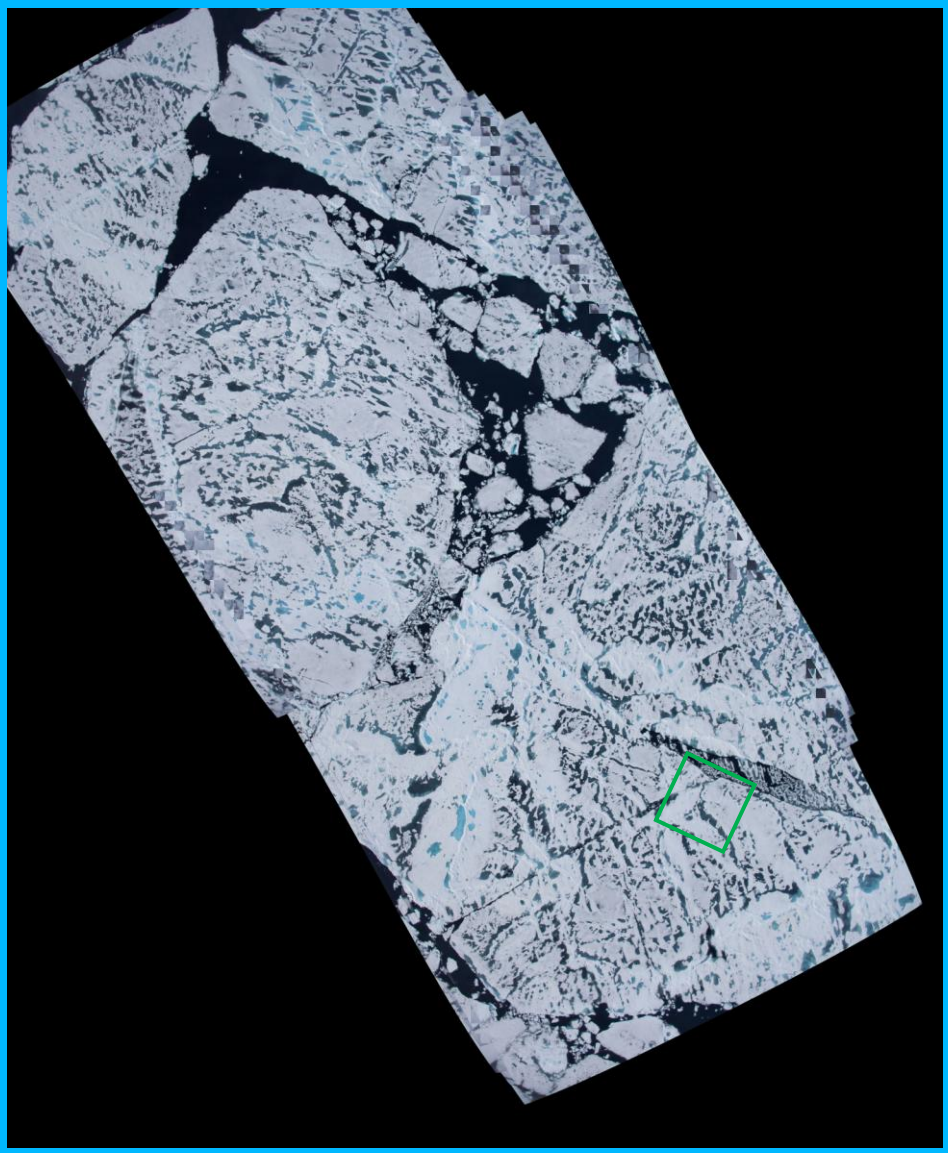

Figure 8 Mosaic of 6 images of sea ice including the ICE12 floe captured from the altitude of about 500 m on 15:12 LT 28.07.12. Prior to merging the images were corrected for lens distortion, vignetting effects and camera altitude and attitude (image rectification procedure). The final image resolution is 0.1 m. The total sea ice area shown in the image mosaic is about 0.95 km^2. The green rectangle approximately outlines the area of the TOPO site shown in Figure 6.

The identified set of objects of two classes is then used for calculating various summary statistics on melt pond configuration, area, open water fraction. The parts of the image not classified as melt ponds/open water were considered bare sea-ice. For the considered area the open water fraction was calculated to be around 3% and the fractional melt pond coverage of 14%.

Figure 10 shows the summary statistics on the areal distribution of melt ponds for the image mosaic displayed in Figure 8**.** The distribution function of melt pond area (not shown here) features a typical heavy-tailed shape. Left panel in Figure 10 showing the estimated cumulative distribution function suggests some 70% of the objects identified as melt ponds are relatively small with the area less than 10 m^2. Yet their cumulative fractional contribution to the surface melt pond coverage as indicated by Figure 10**,** right panel, is less than 10% of the total melt pond covered area. Some 5% of the largest, above 100 m^2, objects identified as melt ponds comprises in turn about 55% of the total melt pond covered area.

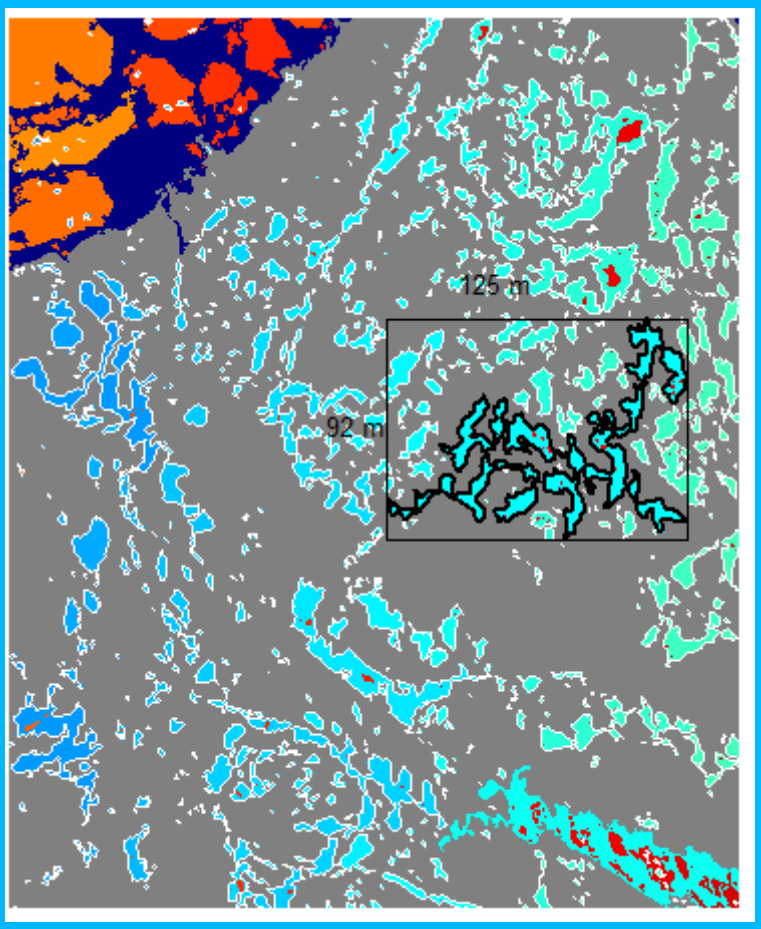

Figure 9. Segment of the ICE12 floe showing the application of the object identification approach applied in this study; white edges highlight objects identified as melt ponds. An example of the system formed by connected melt ponds and identified as a single object of the area of 2000 m^2 is highlighted black bold line. Black solid lines show the bounding box for this object with numbers providing its dimensions. Texture colours used to mark the objects with different reference numbers.

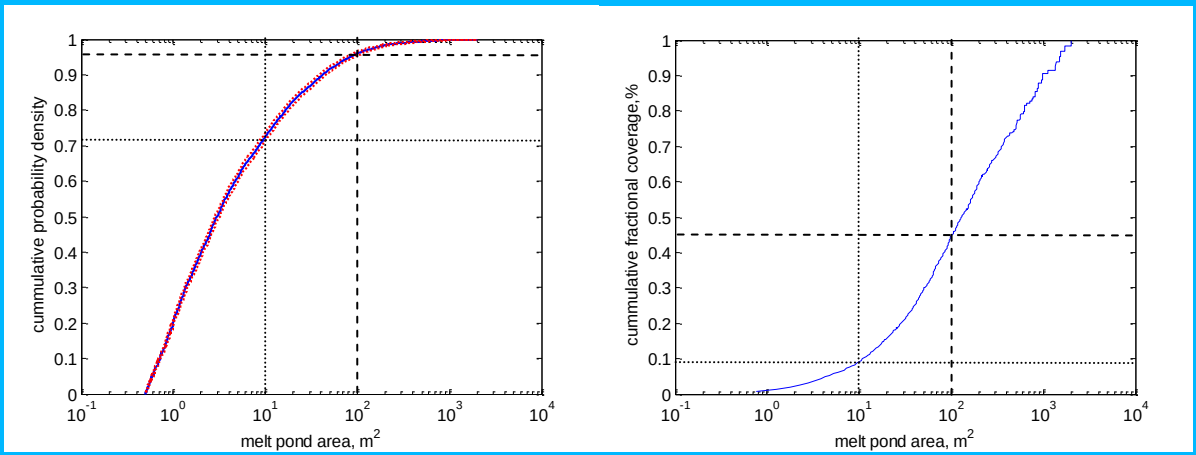

Figure 10, Left panel: Empirical (Kaplan-Meier) estimate of cumulative distribution function of melt pond areas for the ICE12 floe image mosaic shown in Figure 8. Red dotted lines show the 95% confidence interval on the estimate. **Right panel**: Cumulative fractional coverage of melt ponds as a function of melt pond area estimated from the empirical distribution of melt pond areas from the ICE floe image mosaic. The dotted and dashed lines mark the values of the cumulative distribution function and the cumulative fractional coverage corresponding to the melt ponds with the areas of <10 and >100 m^2 referred to in the text.

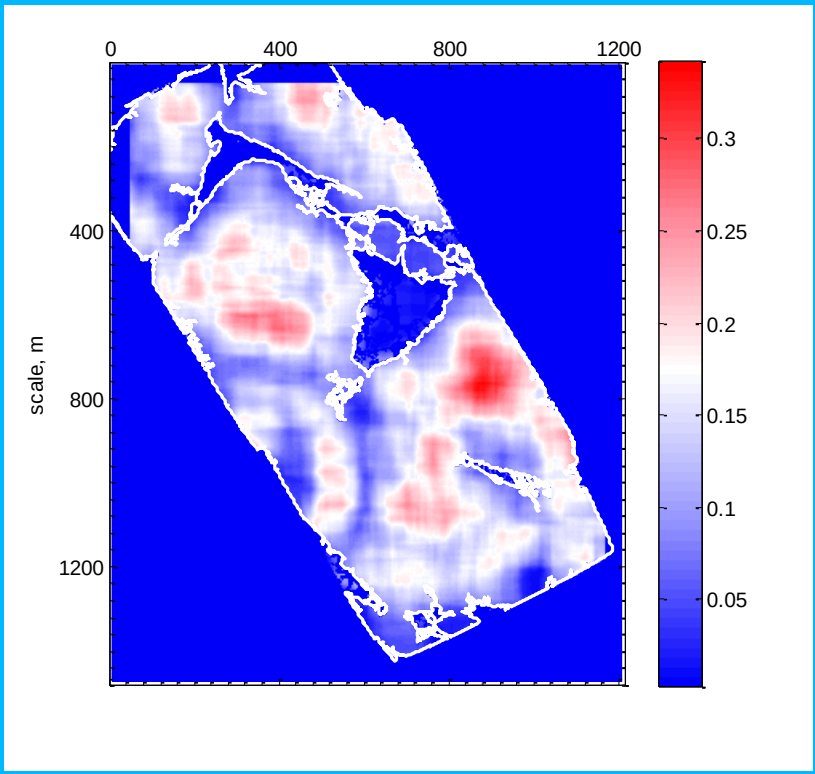

Figure 11. Spatially averaged melt pond coverage calculated using a moving average spatial filter of the width of 1001 pixels. White solid contours highlight the areas identified as open water. Colour bar is for the fractional melt pond coverage.

The spatial distribution of surface melt ponds for the study area is essentially inhomogeneous. We estimated the spatial variability of the melt pond coverage using

rectangular 1001 pixel wide boxcar moving average filter. The footprint of the filter was 100 by 100 m which nearly corresponds to the dimensions of the largest melt pond system identified on the image mosaic. The spatially averaged fractional melt pond coverage was estimated only for the pixels identified as sea-ice or melt ponds. Figure 11 displaying the results of the analysis suggests the melt ponds in the ice station area tend to cluster on sea ice forming some 200 m wide “hot spots” with the areal fraction of melt ponds as high as 35%. These areas are clearly identifiable from the higher resolution images of ICE12 floe as mainly formed of level, undeformed ice. At the same time the ridged segments of ICE12 floe features much lower, below 10% melt pond fractional coverage. The ponds formed on a thicker and ridged ice also have characteristic bright blue colour implying lower surface albedo and light transmissivity of these areas. This was confirmed empirically via measurements of the optical properties of sea ice along transects A-D and T1-3.

The configuration of the melt pond network on level first year ice is also considered to be related with the snow cover topography before the onset of the melt season (Petrich et al., 2012). The initial areal distribution of snow dunes, namely characteristic spatial scale in variability of the snow cover depth preconditions the width of future melt pond channels connected in the network. For every indentified melt pond object its average channel width can be roughly estimated as a ratio of the melt pond area to a longer dimension of the bounding box - the smallest rectangle containing the melt pond. Figure 12 shows the estimated distribution of the channel width for melt ponds larger than 100 m^2 contributing some 55% to the total melt pond covered area.

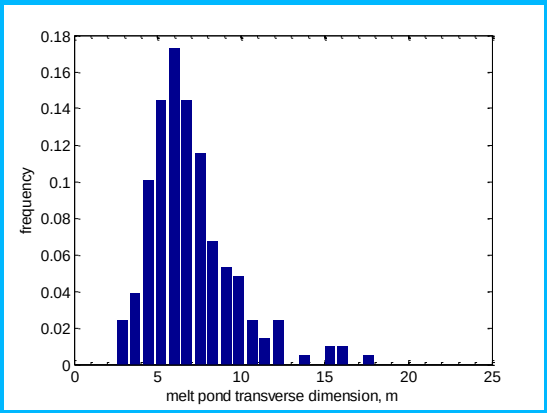

Figure 12. Histogram of the estimated width of melt pond channels for melt ponds exceeding 100 m^2.

Figure 12 suggest the typical width of the melt pond channel to lie within 5-10 m which is much in line with the results of *in situ* mapping (see Figure 6 and Figure 21) and the typical observed length scale of variability in snow cover thickness before the onset of melt season (e.g. Petrich et al., 2012).

4.4. Spatial variability of melt pond coverage inferred from helicopter surveys

This section presents the results of the analysis of sea ice imagery along the four selected flights tracks that took place during ICE12 cruise on 31.07, 01.08, and 02.08.2012. All the flights but one on 31.07 were combined EM-bird/ICE stereocamera flights conditioning the helicopter height of approximately 35 meters above the sea ice surface. This corresponded to a footprint of the images taken by ICE stereocamera system of about 60 × 40 m^2. Note for the two of four flights the flight duration was longer than the camera system memory capacity so these tracks on the figures appear as incomplete.

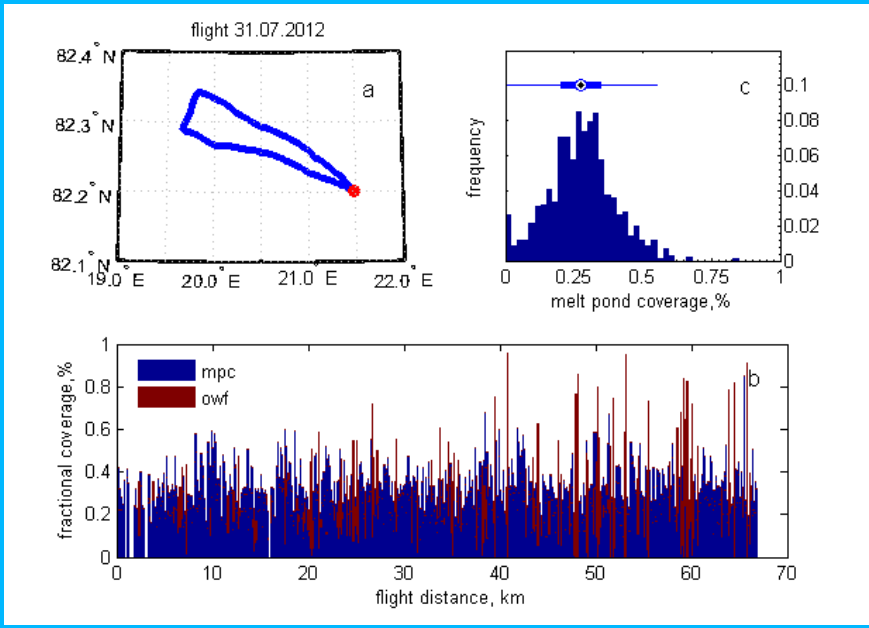

Figure 13. Data summary on the state of sea ice cover from flight on 31.07.2012, GMT time 07:37 – 08:11. (a) flight track; (b) fractional melt pond coverage (mpc) with regard to sea ice area and open water fraction (owf) along the flight track; (c) histogram of mpc and owf along the flight track, average mpc 28% and 25, 50 and 75 percentiles of 20, 28 and 34%, respectively, as shown by Box plot; average owf 5%. The whiskers on Box plot highlight the 1.5 times interquartile range to cover some 99% of the observations in total. With the swath width of 35-40 m, the covered area corresponds to roughly 0.35-0.40 km^2 per 10 km flight track.

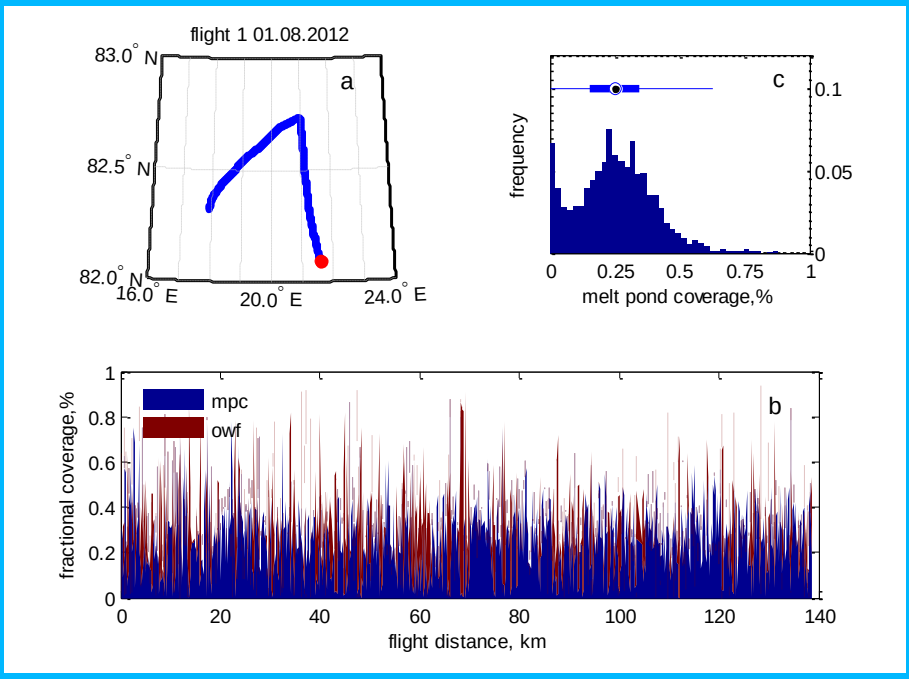

Figure 14. Data summary from flight 1 on 01.08.2012, GMT time 07:23 – 08:35; (a), (b) and (c) panels as in Figure 13**;** average mpc 25% and 25, 50 and 75 percentiles of 15, 25 and 34%, respectively as shown by Box plot; average owf 9%.

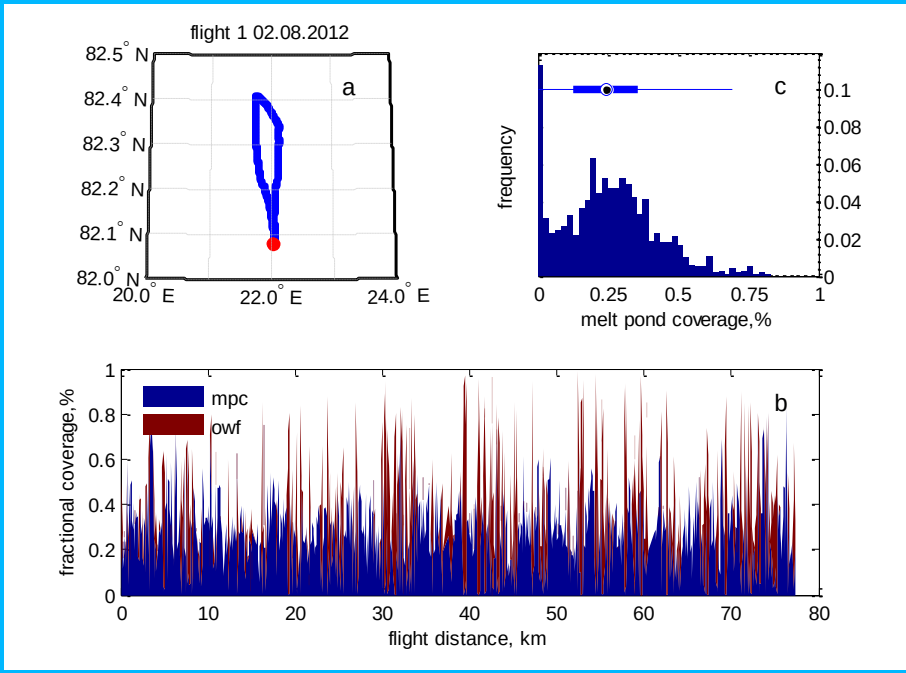

Figure 15. Data summary from flight 1 on 02.08.2012, GMT time 11:22 – 12:00; (a), (b) and (c) panels as in Figure 13; average mpc 25% and 25, 50 and 75 percentiles of 12, 24 and 35%, respectively as show by Box plot; average owf 13%.

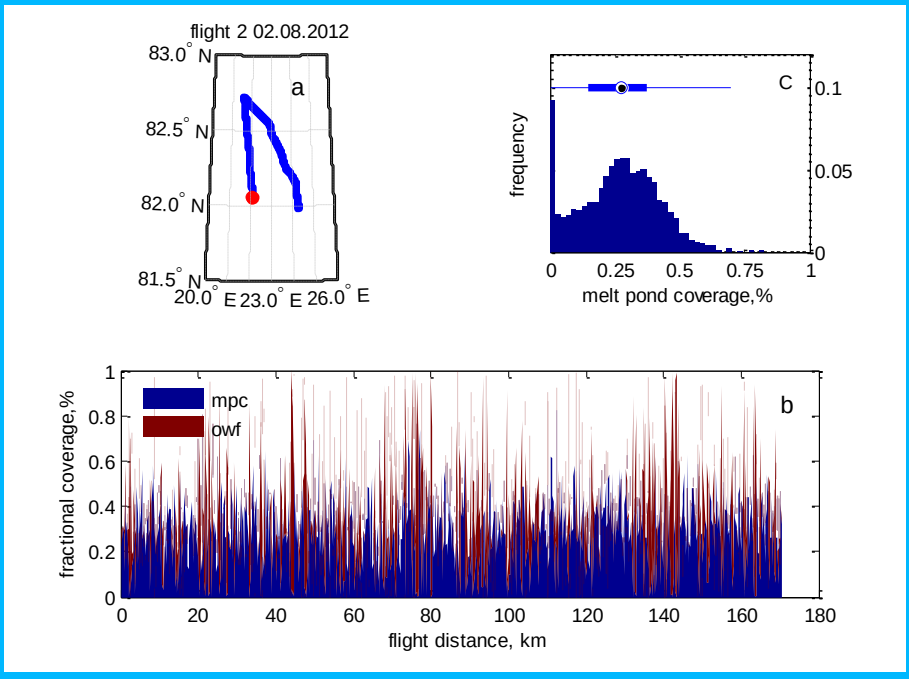

Figure 16. Data summary from flight 2 on 02.08.2012, GMT time 13:22-14:46; (a) flight track; (b) fractional melt pond coverage (mpc) and open water fraction (owf) along the flight track; (c) histogram of mpc and owf along the flight track, average mpc 26% and 25, 50 and 75 percentiles of 15, 27 and 37%, respectively as show by Box plot; average owf 11%.

Figure 13-Figure 16 show the summary statistics on surface melt, and sea ice/open water fractions along the flight tracks. For all the flights the results are much the same with a typical melt pond coverage of about 25% and a similarity in the shapes of the respective probability distributions. The open water fraction varies within 5-13% but this variability lies within the uncertainty of the mean estimates and corresponds well to the respective ice forecast for the area (Figure 3). Notable from the histograms in panels (c) is some 10% frequency of sea-ice images with no melt ponds detected. However, analysis of the respective images suggested this partly could be due to the illumination conditions, specifically the light marks from direct radiation, and hence insufficient for a segmentation contrast of sea ice surface.

4.5. Elements of 3D analysis of sea ice surface topography

We tested the possibility of a 3D reconstruction of sea ice surface topography using the set of photogrammetric calculations applied to the sequence of 18 images captured on 28.07.12 during the surveying flight over the ICE12 floe. The analyzed swath overlaps with the area of the TOPO site and extends some 200 m from the major opening in the center of ICE12 floe towards R/V Lance. The respective segment of the flight track is depicted in Figure 4. The altitude of the camera system above the sea surface varied within 32-34 m during the 17 seconds long swath.

Figure 17 shows the Digital Terrain Model of sea ice surface calculated in SOCET SET with a spatial resolution of 5 cm. The water level was adjusted manually and set to zero using the reference points on the images to ensure the refraction at the water-air interface is properly taken into account.

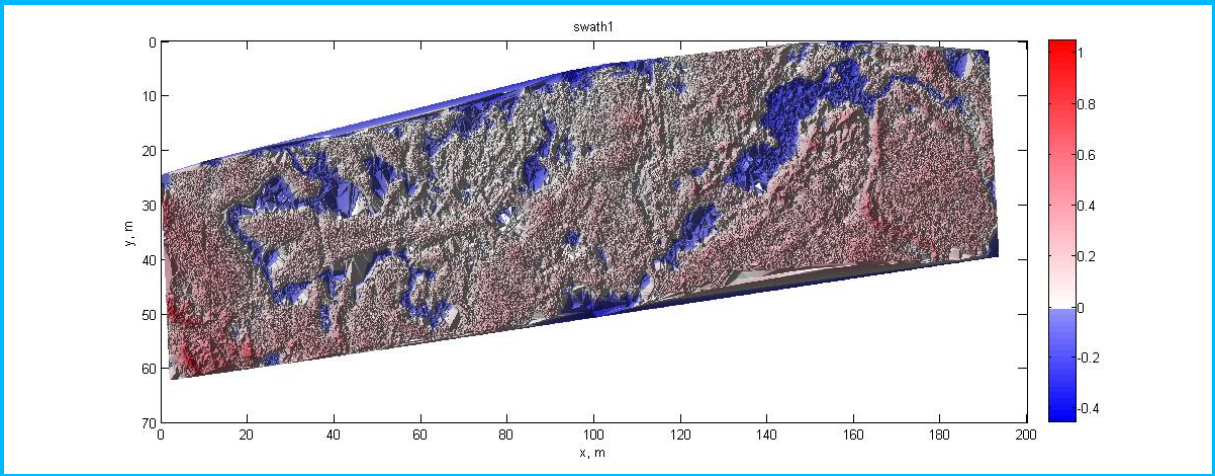

Figure 17. DTM of sea ice surface for the 200 m long swath over ICE12 floe derived from ICE stereocamera images. “Zero” level corresponds to melt pond surface and the sea level. The flight direction is leftwards, from the TOPO site towards *Lance*.

Besides some obvious bias in the edges where the image distortion prevented the algorithm to solve the correspondence problem between the images pairs, the DTM results show a reasonable agreement with the *in situ* TOPO site measurements.

The fractional melt pond coverage for the swath of 20% has some positive bias due to the spurious melt ponds along the edges of the area. The analysis of the melt pond depth distribution for the whole area (see Figure 18, left panel) yields the average pond depth of 9±6 cm only. A somewhat higher value of 12±7 cm average melt pond depth is found for the area with x-values > 100m in Figure 17 that overlaps with a TOPO site location. The shape of the probability distribution (Figure 17, right panel) is similar to the one estimated from *in situ* stake (rotary laser) measurements. Position of the second maximum at around 13 cm, however, suggests the melt ponds inferred from ICE stereocamera system are shallower than they actually were. We hypothesize this could be related with uncertainties in the altitudinal control of the setup and surface water level, with further implications for a correct estimate of the effect of refraction at the air/water interface to the melt pond depths.

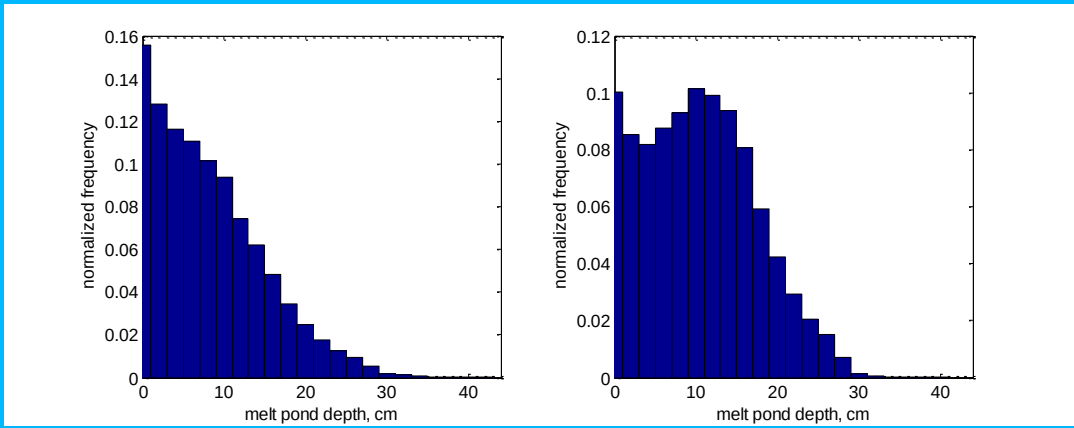

Figure 18. Distribution of melt pond depths along the whole swath from Figure 17 (left) and for the sector of the swath with *x* coordinates >100 m which overlaps with the TOPO site location (right).

Despite some discrepancies this preliminary analysis of the reconstructed 3D scene of the ponded first year ice demonstrates potential of the ICE stereocamera system. A future development of a time efficient workflow for 3D data processing will enable us to acquire extensive data on morphology of summer sea ice surface focusing on a number of features/parameters with a direct relevance for the modeling community. This includes, besides the data on the morphological properties of melt ponds presented here, statistics on surface roughness features like the distributions of ice ridges (e.g. width, height, frequency) or ice floe sizes.

5. Optical characteristics of melt ponds on first year pack ice

5.1 Characteristics of the spatial variability of surface albedo and ice transmissivity from in situ measurements

In order to determine the spatial variability of the albedo the radiation sled observations of the surface radiative fluxes were done on transects representative of the state of sea ice surface in the study area. The measurements were made on 5-m intervals over a total of 490 m at sites A, B, C, D and T1-3 shown in Figure 4. To quantify the radiation transmitted to the ocean, divers also measured the spectral transmittance at the bottom of the ice every meter using *RAMSES-ACC VIS* spectral radiometers (TriOS Mess- und Datentechnik GmbH), along parts of the same transects (total of 99 m on transects T1-3), with an identical sensor measuring incident irradiance at the surface. Note that for these transects the spatial interval of measurements by the sled-based instruments was reduced to 2.5 m.

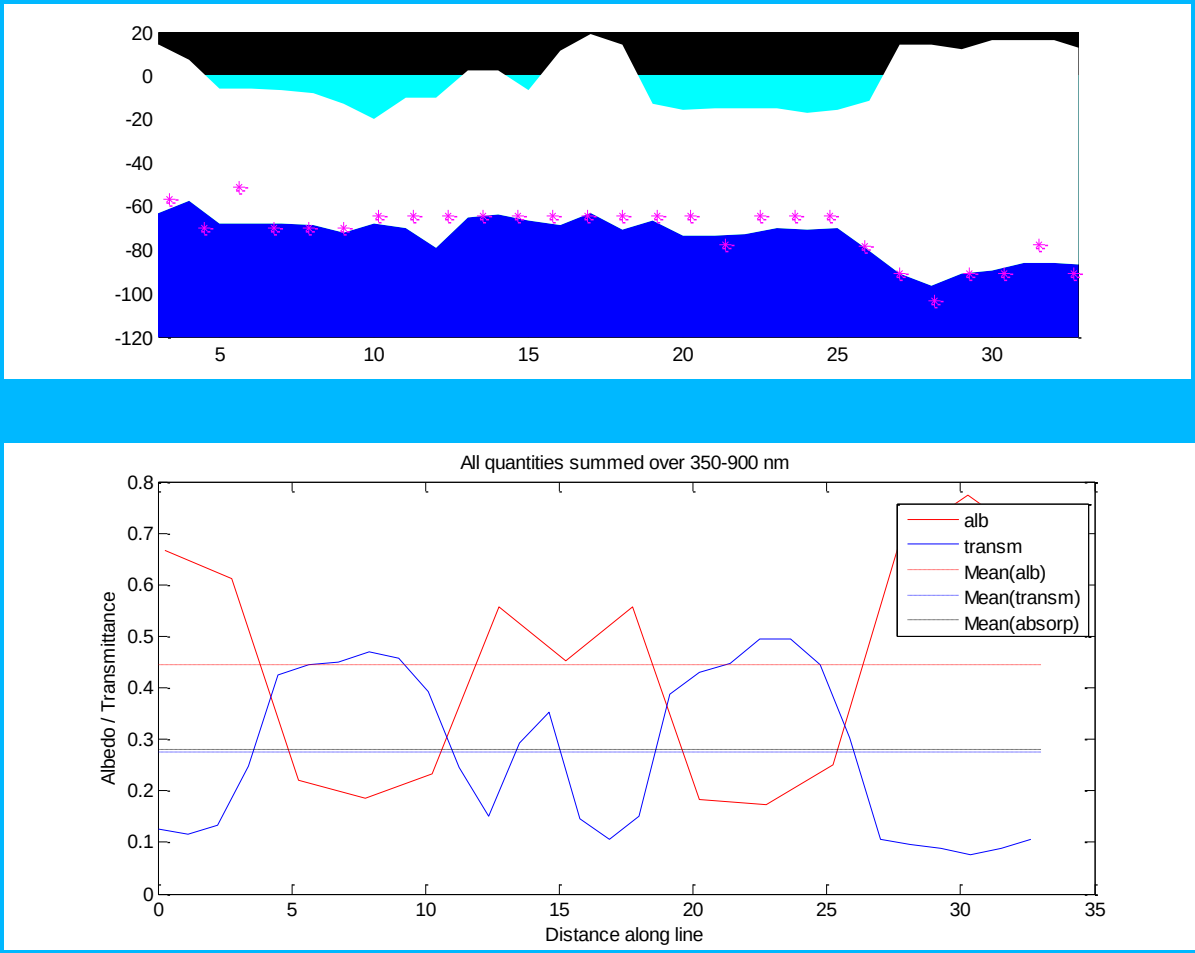

Figure 19 shows the sea ice thickness/melt pond depths profiles along the transmissivity transect T1 together with the respective series of surface albedo and subsurface transmissivity in the band of 350-900 nm. White is for sea ice, light and dark blue are for the melt ponds and the ocean beneath the ice, respectively. In the panels with the albedo/transmittance along the transect variations of the respective quantity shown solid lines, dashed lines are for the transect averages (figures courtesy S. Hudson, NPI).

Manual observations of ice thickness, freeboard and melt pond depth were undertaken every meter along the transmittance transects T1-3. Figure 19 - Figure 21 present the results of the optical measurements for the three transects T1-3 where the parallel measurements of sea ice albedo and transmissivity were carried out.

Results of the observations confirm a crucial role of melt ponds as conduits of solar radiation into the ice slab itself and to the ocean beneath. For the thinner first year ice that was a subject of the summer 2012 field work the presence of well developed melt ponds decreases the surface albedo down to 0.15-0.2 and increases the light transmission through the ice to up to 50-55% of the total incident radiation in the wavelength band of 350-900 nm. The local surface albedo/transmittance obviously depends on sea ice thickness and the melt pond depth but the actual parameterization of this dependence for the collected field data is yet to be determined.

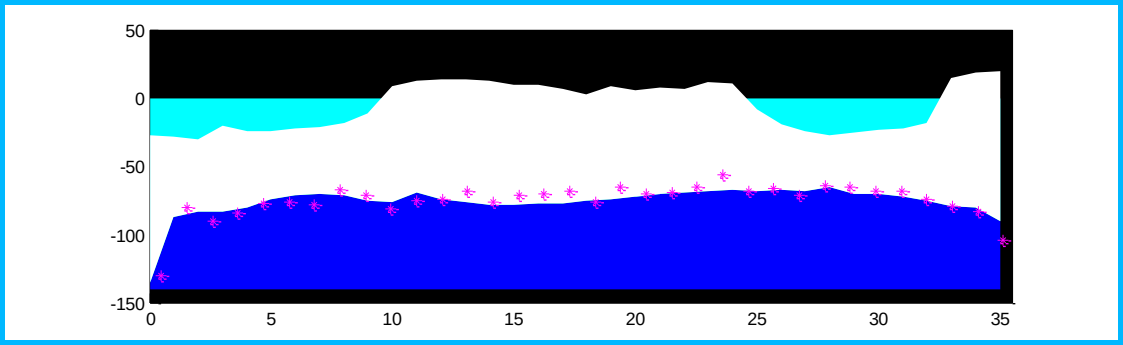

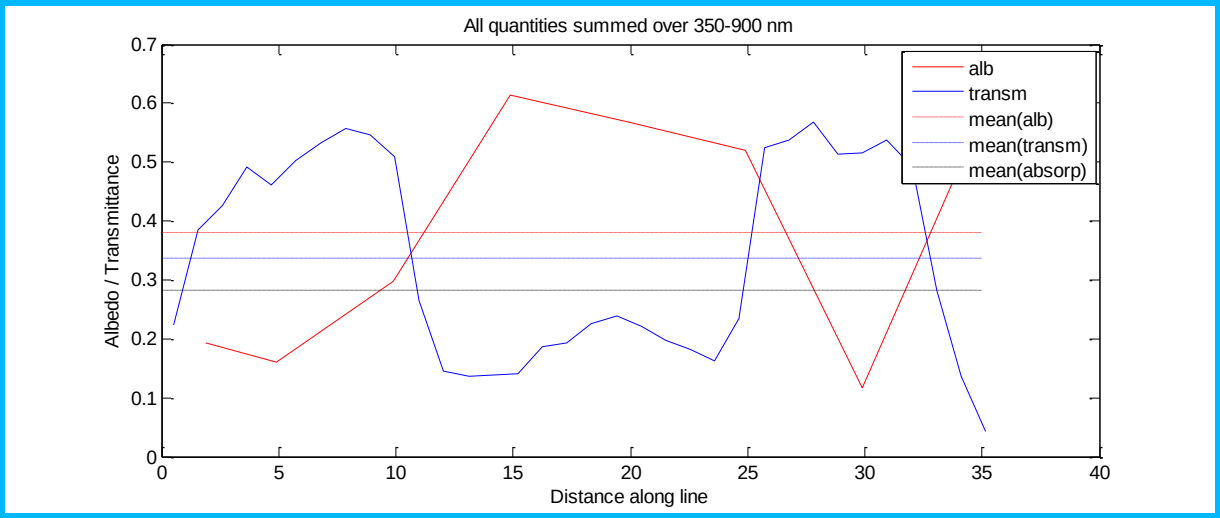

Figure 20. Same as in Figure 19 for but for transect T2

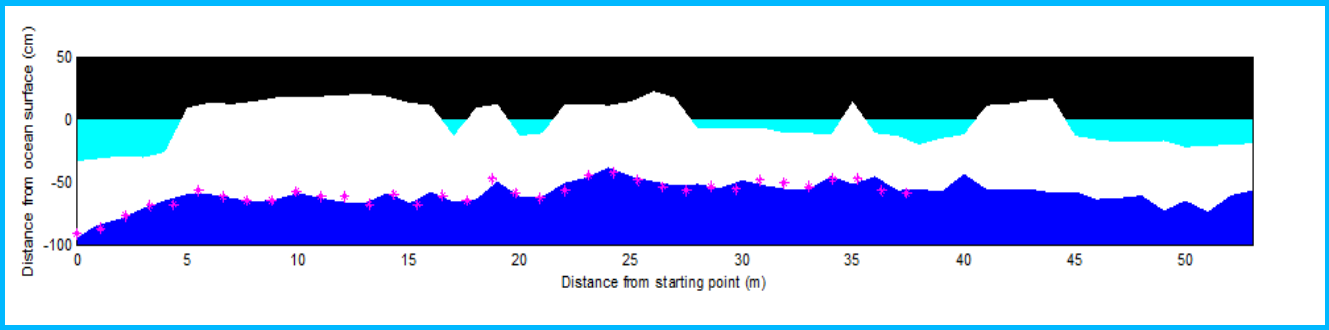

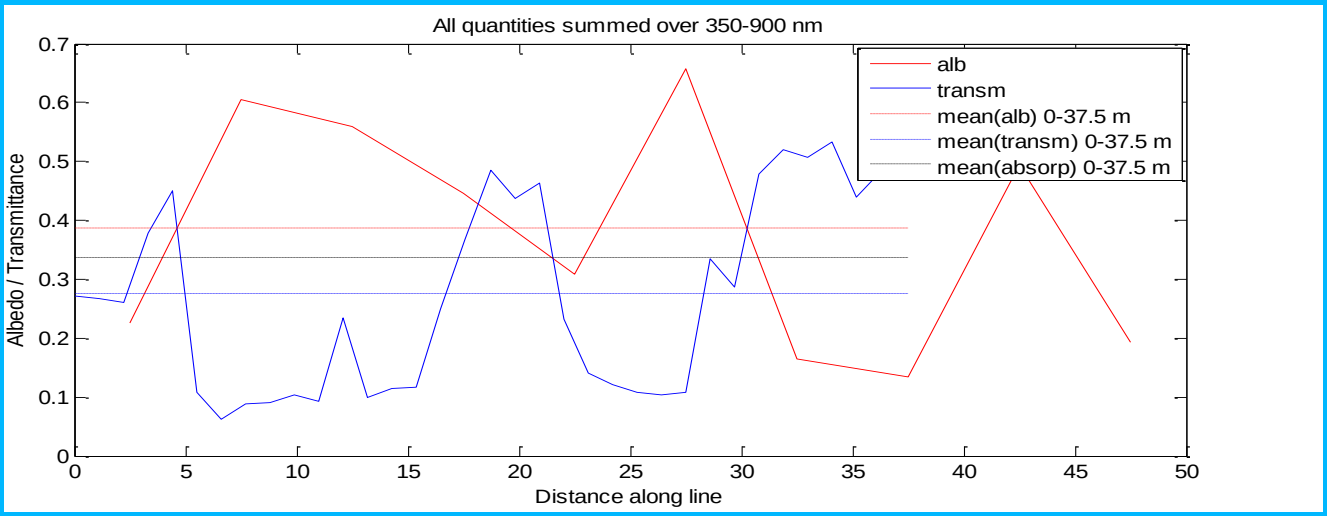

Figure 21. Same as in Figure 19 but for transect T3.

5.2 Spatial aggregate scale albedo from in situ and helicopter borne imagery

Surface photos and measured properties along the transect lines were then used to identify and group the measurements into three different categories of surfaces: white ice (bare ice with surface scattering layer), dark ponds, and light ponds (light blue ponds with thicker, more reflective ice underneath). Using these subsets of observations, the average albedo and transmittance of these ice types were determined. Table 2 presents the summary statistics on the optical measurements on ICE12 floe.

Surface type	Albedo	Transmittance
Open water	0.07	0.93
White ice	0.55	0.11
Bright pond	0.34	0.20
Dark pond	0.15	0.39

Table 2 The calculated mean broadband albedo and transmittance of first year Arctic sea ice for each surface type within the study area.

For the ratio of “dark” ponds to “bright” ponds of about 2/1 identified from ICE12 floe image mosaic using the technique of Renner et al., (2013), and a known total fractional melt pond coverage of 14% and open water fraction of 3%, an aggregate albedo [Perovich et al., 2005] of the ICE12 floe area was estimated to be around 0.48.

Figure 22 and Figure 23 present similar estimates made for the data on sea ice state inferred from the helicopter imagery along the four selected flights presented earlier in Section 4.4. The results are further summarized in Table 3.

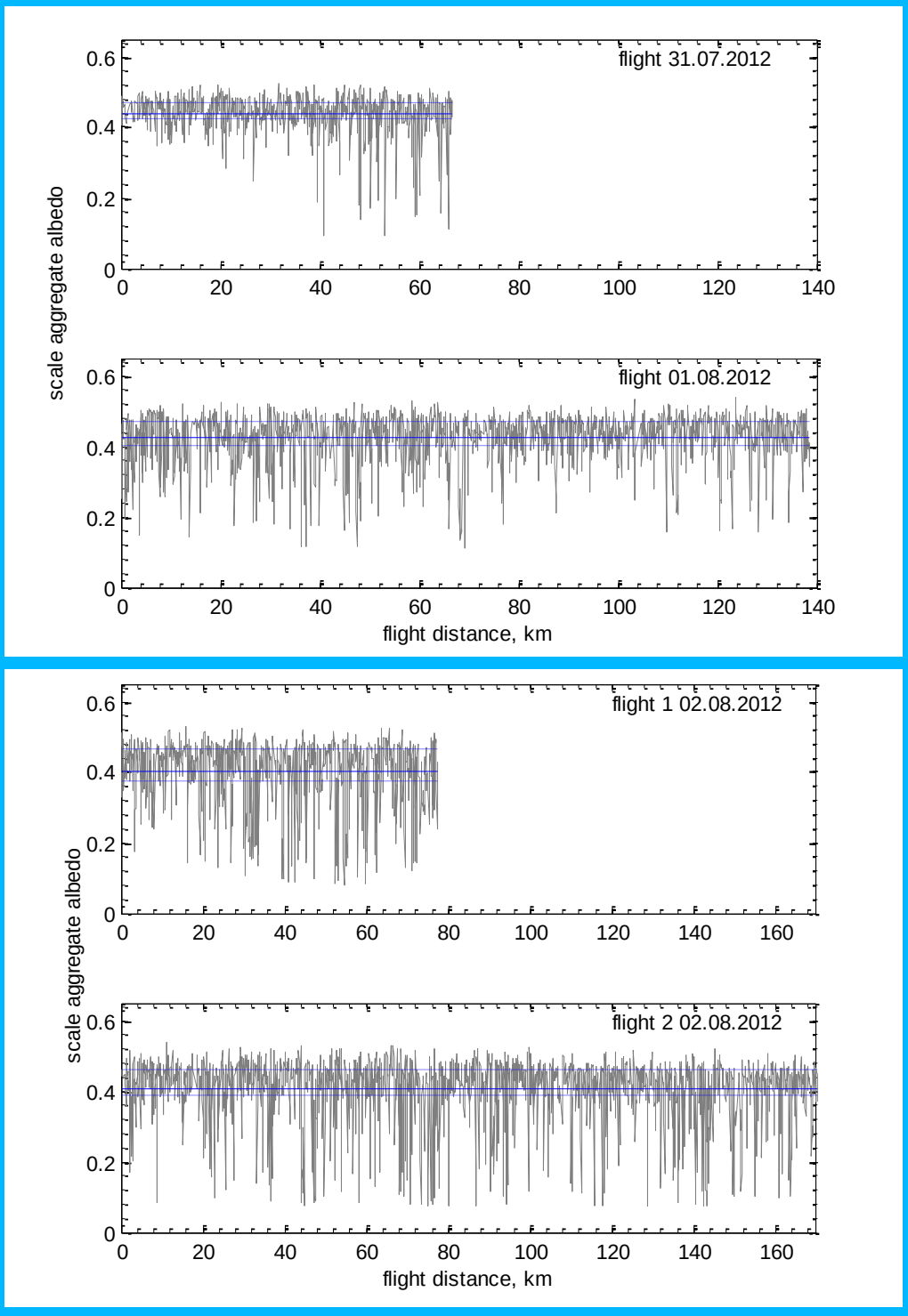

Figure 22 Aggregate scale surface albedo along the four ICE12 cruise helicopter flight tracks presented in Section 4.4 in Figure 13 - Figure **16**. Solid blue line is for the track averaged albedo, dashed lines show the 25 and 75 percentiles of the respective distribution. Note skewness of the distribution towards lower albedo values and asymmetric position of the mean with respect to the 25 and 75 percentiles. With the swath width of 35-40 m, the covered area corresponds to roughly 0.35-0.40 km^2 per 10 km flight track.

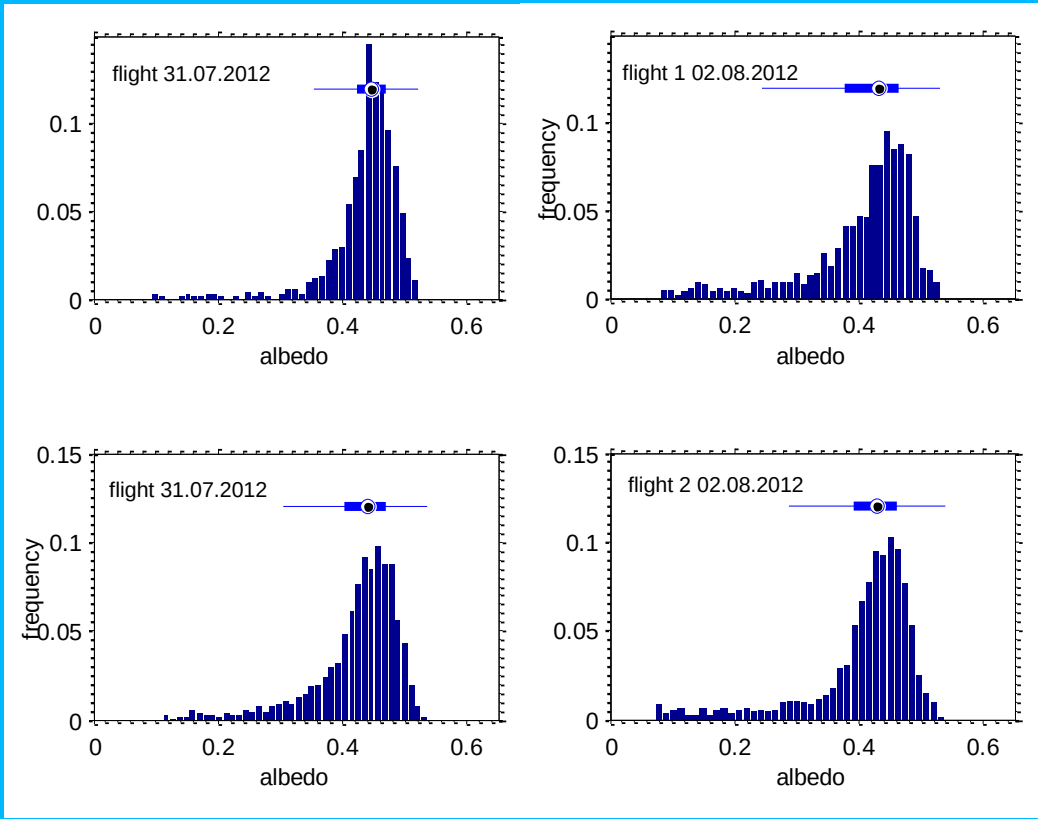

Figure 23 Histograms of aggregate scale surface albedo along the flight tracks from Figure 13 - Figure **16**. The Box plot on the top of each panel highlights the meadian, the interquartile (25-75) range and 1.5 times interquartile range to cover some 99% of the observations in total.

Table 3 Summary statistics on the state of sea ice cover and scale aggregate surface albedo with the respective standard deviations along the four helicopter flight tracks from ICE12 cruise.

Helicopter track	Transect length, km	Open water coverage, %	Melt pond fraction, %	Average aggregate scale albedo
31.07.12	67	5	28	0.44(0.05)
01.08.12	139	9	25	0.42(0.07)
02.08.12,flight 1	78	13	25	0.40(0.09)
02.08.12,flight 2	170	11	26	0.41(0.09)

Figure 22 and Figure 23 indicate that both the averaged aggregate scale surface albedo and its probability distribution are fairly stable between the flight tracks pointing to a similar state of sea ice cover in the area of some 80 km around the mean position of the ice floe during the ICE12 cruise drift. The albedo probability distributions presented in Figure 24 are skewed substantially towards zero due to the presence of open water areas. It suggests that the spatially averaged regional scale surface albedo of melting sea ice pack estimated from a

sequence of smaller scale images can be negatively biased. This may have implications for the areal estimates of the surface energy budget both in observational and modelling studies. The actual magnitude of the effect as well as the impacts of these "subgrid-scale" features on the validation of remote sensing and model data requires further analysis.

6. Conclusions

In this report we presented some of the results of the data analysis on the features of sea ice surface topography during melt. The data were collected in summer 2012 (specifically 26.07-03.08) in the higher Arctic to the north of Svalbard at 82.5°N. Detailed mapping of the sea ice surface was done via combination of the on ice work using the rotary laser and stake measurements and the helicopter born imagery using the recently developed ICE stereocamera system. The use of EM-bird instrument to measure the thickness of the ice during the ice reconnaissance flights in parallel with the camera system conditioned the typical flight altitude of about 35 m along the flight tracks and the typical swath width of about 35-40 m. However, additional overview flight at some 500 m altitude over the ice station floe provided the data on the larger scale features of the spatial distribution of melt ponds in the study area. In parallel to the study of the morphological properties of sea ice surface we conducted a series of measurements on the optical properties of melting first year ice. As the major focus of the work was on melt ponds, namely their morphological and optical properties, we presented the relevant statistics on the melt pond coverage, aerial distribution, depths and albedo/transmissivity for bare and ponded first year ice.

The report highlights are listed below:

1) Combined results of the on-ice work and aerial surveys demonstrate that the first year ice in the study area was in the advanced stage of melt. The modal ice thickness as inferred from the aerial surveys using the EM instrument was about 0.8 m and fraction of open water was less then 0.1. By the time of the field campaign the snow cover has melted away and the melt pond coverage attained some 15% on the larger ice floe where we established the ice station. Analysis of the sea ice imagery along the four selected helicopter flights tracks of about 250 km in total in the study area, suggests even higher melt pond coverage with an average value of about 25%. Both estimates, however, lie within the inferred natural variability of this value.
2) Analysis of the image mosaic comprising the scene of about 1 km^2 including the area of the drift ice station floe suggest the melt ponds on ice pack may tend to cluster forming "hot spots" with the areal fraction of surface melt as high as 35%. These areas are mainly formed of level, undeformed ice. The ridged segments of ICE12 floe featured much lower, below 10% melt pond fractional coverage. The ponds formed on this thicker and ridged ice also had a characteristic bright blue colour implying lower surface albedo and light transmissivity of these areas.
3) Stake measurements of melt pond depths on a regular grid at the topography site as well as along the transects revealed the pond depth to vary within 0-28 cm. Although the mean depth of 10 cm was found for the TOPO site, the actual probability distribution appeared to be bimodal. The first peak of about 5 cm water depth was associated mainly with the newly formed ponds, and ponds filled with a slush, while for the well developed ponds connected to the ocean we registered a typical depth of 15-20 cm. We found a similar range of depths for the well developed ponds along the transects where the optical measurements were conducted.

4) Optical measurements along the three transects using the mobile instrument platform revealed the typical surface broadband albedo of dark/bright ponds of 0.15/0.34 respectively and for the bare first year ice of 0.55. Note these values are valid for the period of melt and relatively thin ice we studied during the summer field campaign.
5) Estimates of the mean aggregate scale albedo along the four flight tracks yielded values in the range of 0.41-0.44, similar to within the respective uncertainties. The surface albedo probability distributions along the flight tracks are however skewed towards zero due to the presence of open water areas. It suggests that the spatially averaged regional scale surface albedo of melting sea ice pack estimated from a sequence of smaller scale images can be negatively biased with the correspondent implications for the areal estimates of the surface energy budget.

The summary for some of the data collected in 2010 campaigns in the Arctic to the north of Svalbard and in the Fram Strait have been recently published in [Renner et al., 2013]. More results including a detailed analysis of the energy budget of melting first-year ice inferred from 2012 on ice field work to the north of Svalbard are summarized in [Hudson et al., *accepted*]. As the data processing and analysis is an ongoing process, more results for 2011 and 2012 field campaigns are planned for release in our future publications.

References

Gonzalez, R. C., R. E. Woods, and S. L. Eddins, 2004, *Digital Image Processing Using MATLAB*, New Jersey, Pearson Prentice Hall.

Hudson, S.R., Granskog, M.A., Karlsen, T.I. and K. Fossan, 2012: An integrated platform for observing the radiation budget of sea ice at different spatial scales, *Cold Regions Science and Technology*, 82, 14-20, doi:10.1016/j.coldregions.2012.05.002.

Hudson, S.R., Granskog, M.A., A. Sundfjord, A. Randellhof, A.H.H. Renner, D.V. Divine, 2013: Energy budget of first-year Arctic sea ice in advanced stages of melt, accepted for publication in *Geophysical Research Letters*.

Perovich, D. K., 2005: On the aggregate-scale partitioning of solar radiation in Arctic sea ice during the Surface Heat Budget of the Arctic Ocean (SHEBA) field experiment, *J. Geophys. Res.*, 110, C03002, doi:10.1029/2004JC002512.

Petrich, C., H. Eicken, C. M. Polashenski, M. Sturm, J. P. Harbeck, D. K. Perovich, and D. C. Finnegan, 2012: Snow dunes: A controlling factor of melt pond distribution on Arctic sea ice, *J. Geophys. Res.*, 117, C09029, doi:10.1029/2012JC008192.

Renner, A.H.H., Dumont, M., Beckers, J., Gerland, S. and C. Haas, 2012: Improved characterisation of sea ice using simultaneous aerial photography and sea ice thickness measurements, *Cold Regions Science and Technology*, 10.1016/j.coldregions.2013.03.009.

Renner, A. , Hendricks, S. , Gerland, S. , Beckers, J. M. , Haas, C. and Krumpen, T. 2013: Large-scale ice thickness distribution of first-year sea ice in spring and summer north of Svalbard , *Annals of Glaciology*, 54 (62) . doi: 10.3189/2013AoG62A146

Otsu, N., 1979: A Threshold Selection Methodfrom Gray-Level Histograms, *IEEE Transactions on Systems, Man, and Cybernetics*, 9(1), 62-66.